Deepti Hariharan, Kanikode Abdul Latheef Abdul Rahman
Group P3

Advanced Lab Course: Analysis of Z^0 Decay (E213)

Contents

1. Introduction

Data from the e^+e^- collisions with the Omni-Purpose Apparatus LEP (OPAL) detector at the Large Electron-Positron (LEP) collider storage ring was analyzed to measure the parameters of Z^0 decay. First, event displays of individual decay channels were analyzed to get a qualitative idea of the different decays and to determine crude cuts. Next pure samples were analyzed with the help of Monte Carlo simulation which helped in optimizing the cuts. Finally, these cuts were applied to real data and the cross-sections of different decay channels of Z^0 was measured. The forward-backward asymmetry for muon decay channel and the number of generations of light neutrinos was also calculated.

2. Theory

2.1. The Standard Model

The Standard Model of particle physics is a theoretical framework describing the elementary particles and their interactions. It explains three of the four fundamental forces; namely weak interaction, strong interaction and electromagnetic interaction. Elementary particles are classified based on their spin as fermions (half-integer spin) and bosons (integer spin) based on their spin (fig. 2.1). Fermions are further classified into three generations of quarks and leptons. The gauge bosons (spin 1) act as mediators. The Higgs boson is part of the Higgs mechanism which explains why particles have mass on the basis of spontaneous symmetry breaking.
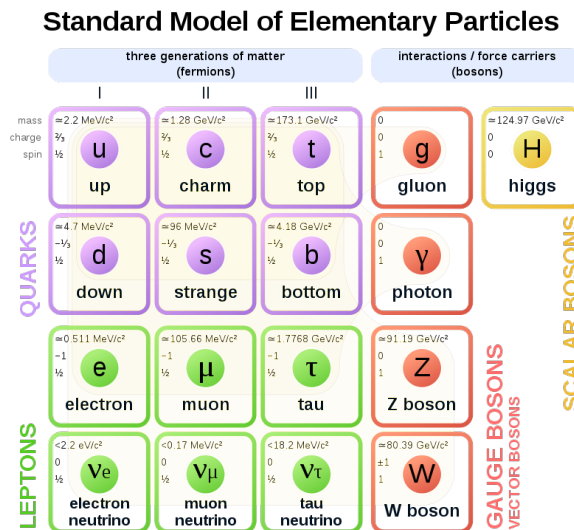
Figure 2.1.: Standard Model of Particle Physics (source: Wikipedia, author: MissMJ)

2.2. Electroweak Theory

Quantum electrodynamics (QED) explains the interaction between charged particles mediated by photons (γ). It was explained by the symmetry group U(1) with the field quantum Y^0, analogous to photons. The weak interaction initially predicted the massless W^+, W^- and W^0 bosons by means of SU(2) symmetry.

It was found that weak and electromagnetic interactions have similar coupling strengths at high energies. This led to their unification by means of the SU(2) × U(1) symmetry with the four generators W^+, W^-, W^0 and Y^0. It was observed that Y^0 did not couple with neutrinos meaning it is not identical to photons. Therefore, it was assumed that the photon field is a quantum mechanical mixture of Y^0

and W^0 perpendicular to the photon field giving rise to the Z^0 boson. The mixing angle, called the Weinberg angle (θ_W) is such that:

$$\begin{pmatrix} \gamma \\ Z^0 \end{pmatrix} = \begin{pmatrix} cos\theta_W & sin\theta_W \\ -sin\theta_W & cos\theta_W \end{pmatrix} \begin{pmatrix} Y^0 \\ W^0 \end{pmatrix} \tag{2.1}$$

2.3. Physics at Energies Near Z^0 Resonance

Z^0 are produced as virtual particles during e^+e^- scattering and decay into a fermion-antifermion ($f\bar{f}$) pair. If the center-of-mass energy of the initial state particles is near the Z^0 mass, real Z^0 particles can be produced and the cross-section is resonant [1]. The total decay width of Z^0 is the sum of all partial decay widths:

$$\Gamma_{Z^0} = \Gamma_e + \Gamma_\mu + \Gamma_\tau + \Gamma_{hadron} + \Gamma_\nu \tag{2.2}$$

The number of generation of light neutrinos can be determined using this equation. The lowest order Feynman diagram for the process $e^+e^- \longrightarrow f\bar{f}$ is shown in fig. 2.2 The cross-section is given by:
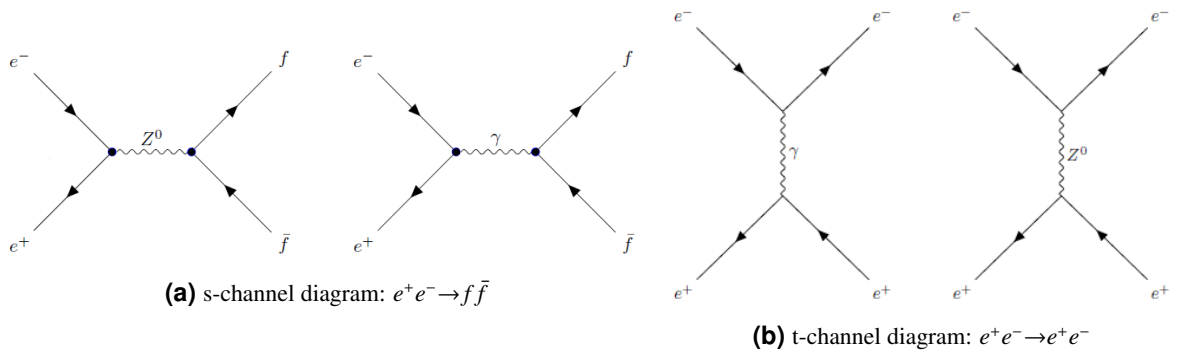
$$\sigma(e^+e^- \to f\bar{f}) = \sigma_{Z^0} + \sigma_\gamma + \sigma_{Z^0\gamma} \tag{2.3}$$

At the Z^0 resonance, the cross-section is dominated by σ_{Z^0} which follows the Breit-Wigner distribution for spin 1 particles:

$$\sigma_f = \frac{12\pi \cdot \Gamma_e \cdot \Gamma_f}{s \cdot M_{Z^0}^2} \cdot |\chi(s)|^2 = \frac{12\pi}{M_{Z^0}^2} \cdot \frac{s \cdot \Gamma_e \cdot \Gamma_f}{(s - M_{Z^0}^2)^2 + (s^2 \frac{\Gamma_{Z^0}^2}{M_{Z^0}^2})} \tag{2.4}$$

where s is the square of center-of-mass energy. Near the Z^0 resonance, $s = M_{Z^0}^2$ and the cross-section reduces to:

$$\sigma_f^{peak} = \frac{12\pi}{M_{Z^0}^2} \frac{\Gamma_e}{\Gamma_{Z^0}} \frac{\Gamma_f}{\Gamma_{Z^0}} \tag{2.5}$$

(a) s-channel diagram: $e^+e^- \to f\bar{f}$

(b) t-channel diagram: $e^+e^- \to e^+e^-$

Figure 2.2.: Lowest order Feynman diagram for e^+e^- scattering [1]

The s-channel is dominant for large scattering angles $\left(\frac{d\sigma_{(s)}}{d\Omega} \propto (1 + cos^2\theta) \right)$ and for small angles, t-channel is dominant $\left(\frac{d\sigma_{(t)}}{d\Omega} \propto (1 - cos^2\theta)^{-2} \right)$.

2.3.1. Forward-Backward Asymmetry A_{FB}

The differential cross section for the reaction $e^+e^- \rightarrow \mu^+\mu^-$ in lowest order perturbation theory is not symmetric with respect to the scattering angle (angle between incoming e^+ and outgoing μ^+). The cross-sections in the forward and backward hemispheres determine the asymmetry.

$$A_{FB}^f = \frac{\int_0^1 \frac{d\sigma}{d\cos\Theta} d\cos\Theta - \int_{-1}^0 \frac{d\sigma}{d\cos\Theta} d\cos\Theta}{\int_0^1 \frac{d\sigma}{d\cos\Theta} d\cos\Theta + \int_{-1}^0 \frac{d\sigma}{d\cos\Theta} d\cos\Theta} \tag{2.6}$$
$$= \frac{3}{4}\frac{F_2}{F_1}$$

If the center-of-mass energy is exactly on the resonance maximum ($\sqrt{s} = M_{Z^0}$), for leptons, A_{FB} reduces to:

$$A_{FB}^{l,peak} \simeq 3\,(1 - 4sin^2\theta_W) \tag{2.7}$$

We can then determine the Weinberg angle, $sin^2\theta_W$ from A_{FB} at the resonance maximum.

2.4. The OPAL Experiment

OPAL (Omni Purpose Apparatus for LEP) was one of the four detectors at LEP. Its construction is shown in fig. 2.3.
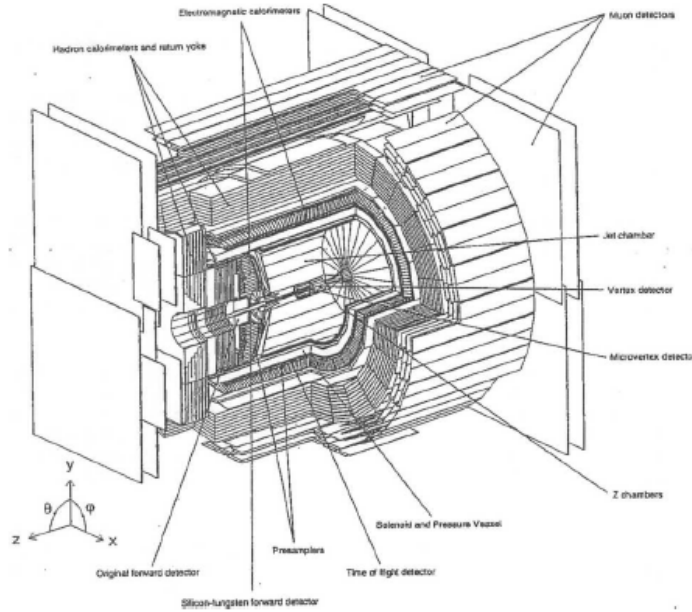

Figure 2.3.: The OPAL detector [1]

2.4.1. The OPAL Detector

The central detector is built cylindrically surrounding the collision point. The μ-vertex-detector is closest to the origin. It is a semiconductor detector with silicon chips. This is surrounded by the vertex chamber–a multiwire proportional counter. Next is the jet chamber, composed of wires parallel to the

beam axis and it detects the *r* and *φ* components. The next layer is the Z-chamber which has wires radial to the beam axis and detects the *z* component. The whole device is situated inside and autoclave consisting of 88.2% argon, 9.8% methane and 2% isobutane at a pressure of 4 bar. A solenoid of length with magnetic field 0.435T, parallel to the beam surrounds the tank. The solenoid is followed by a time-of-flight (TOF) system in the radial direction which consisting of 160 scintillation counters. The scintillation light is detected at the beginning and the end of the device and the output of the TOF system triggers the detector and measures the flight time of the particles. The presampler consisting of 16 steamer chambers is situated around the TOF system. This is followed by the electromagnetic calorimeter made up lead glass blocks to detect the electron shower. The forward detectors (FCAL) are present at the endcaps of the electromagnetic calorimeter and measure the Bhabha scattering by detecting coinciding e^+e^- pairs to measure the luminosity. The hadronic calorimeter (HCAL) is present outside the solenoid serving as a flux return for the magnetic field and detects the hadron shower. Four layers of muon chambers (MUON) are installed outside HCAL.

2.4.2. Particle Identification

Particles are classified into charged and uncharged particles. The charged particles have visible tracks in the detector due to Cherenkov effect. The signature shower of electrons and charged hadrons differ in terms of the energy and location. Muons do not have a shower as they penetrate bulky matter. At low energies (below 2GeV), the hadronic and electronic showers are indistinguishable and differentiation is done by the energy loss dE/dx in the jet chamber. Different neutral particles have different shower profiles. Pions decay into two photons with V-shaped trajectories. Neutral hadrons with large flight time are identified by hadronic showers. The schematic representation of the signature of elementary particles at OPAL is shown in fig. 2.4.
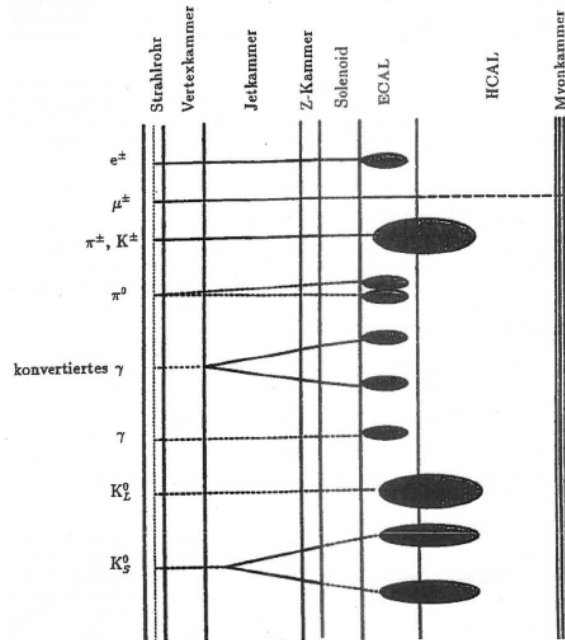
Figure 2.4.: Schematic representation of the signature of elementary particles at OPAL [1]

3. Identification of Particles and Classification of Events

The global variables used in this experiment as as defined below:

- Ncharged: Number of tracks of charged particles of an event found in the tracking chamber

- Pcharged: Scalar sum of momenta of all charged tracks of an event measured in the vertex/jet/Z-chambers

- E_ecal: Total energy of an event measured in ECAL

- E_hcal: Total energy of an event measured in HCAL

3.1. Measurements and Cuts

Different events of the decay channels vary in some or all of the above mentioned variables. These are separated by making a cut on the required variable. The cut is chosen in a way that maximum portion of the desired events fall under the required criterion and background is minimum. The acceptance (efficiency) of the cut is given by the ratio of the events that fulfill the criterion and the total number of events.

3.2. Monte-Carlo Simulation

Calculation of the cross-section requires the exact number of events of the particular class. Cuts reduce the accuracy in the number of observed events N_{obs} and it has to be corrected. Since the experiment gives only the sum of all events, this cannot be done with only the experiment results and therefore simulations are used.
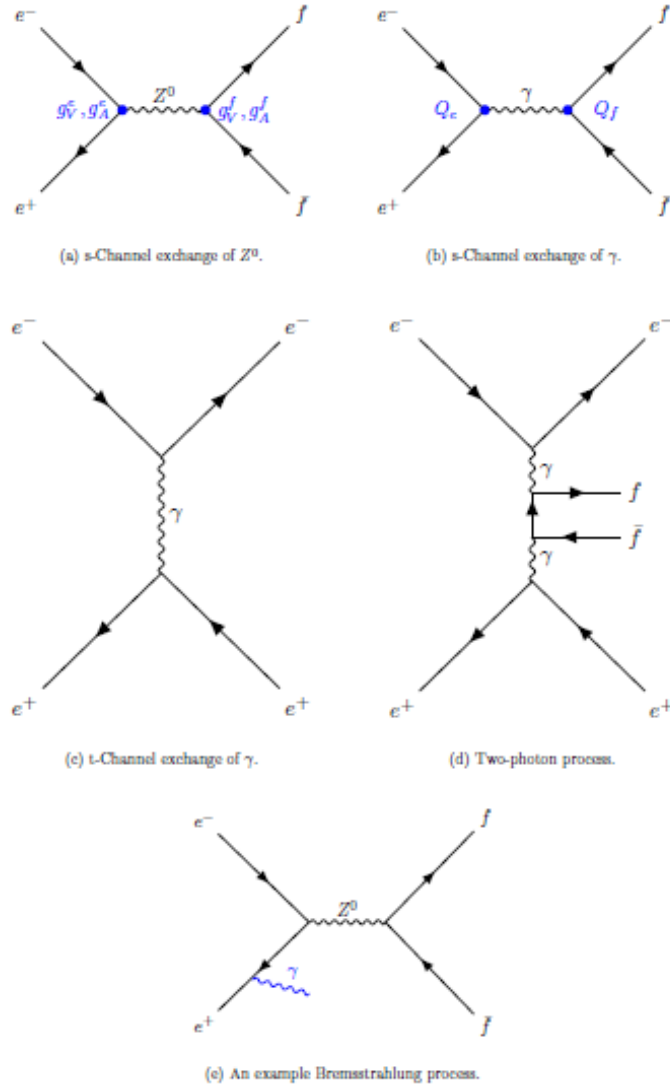
The elastic scattering of fermion-antifermion (e^+e^-) pair and the decay of subsequent unstable particles (Z^0) is simulated. All detector signals from the traversing particles are included in the simulation to resemble the real detector environment. Simulations contain details about the particles and information contained in the real data. It can be used to study the detector output with respect to particular events.

3.3. Classification of Z^0 events

3.3.1. Decay Channels of e^+e^-

$e^+e^- \rightarrow e^+e^-$

The processes that contribute at lowest order are shown in fig. 3.1 a, b and c. The t-channel process has high cross-section at small scattering angles and is used to calculate the luminosity (fig. 3.2 a).

(a) s-Channel exchange of Z^0.

(b) s-Channel exchange of γ.

(c) t-Channel exchange of γ.

(d) Two-photon process.

(e) An example Bremsstrahlung process.

Figure 3.1.: Feynman diagrams of import e^+e^- processes [1]

The e^+e^- events are identified with high energy deposited in the ECAL. The s-channel events can be isolated with a cut on the scattering angle.

$e^+e^- \rightarrow \mu^+\mu^-$

The muons penetrate the ECAL and HCAL and are detected only in the muon chamber. These events are identified by a cut on the momentum of charged tracks and energy deposited in ECAL.

$e^+e^- \rightarrow \tau^+\tau^-$

τ is unstable and decays via multiple decay channels which have different number of prongs of decay, i.e., the number of charged particles produced by the decay. fig. 3.2 c shows a $Z^0 \rightarrow \tau^+\tau^-$ event with a tau decaying into and electron and two neutrinos.

$e^+e^- \rightarrow \nu\bar{\nu}$

These are invisible decay modes and can be measured only by selecting events with a single photon from the initial state radiation.

$e^+e^- \rightarrow q\bar{q}$

The charged multiplicity of hadronic events is greater than leptons (fig. 3.2 d). The two-photon reactions (fig. 3.1 d) is a possible additional background for the hadronic decay mode.
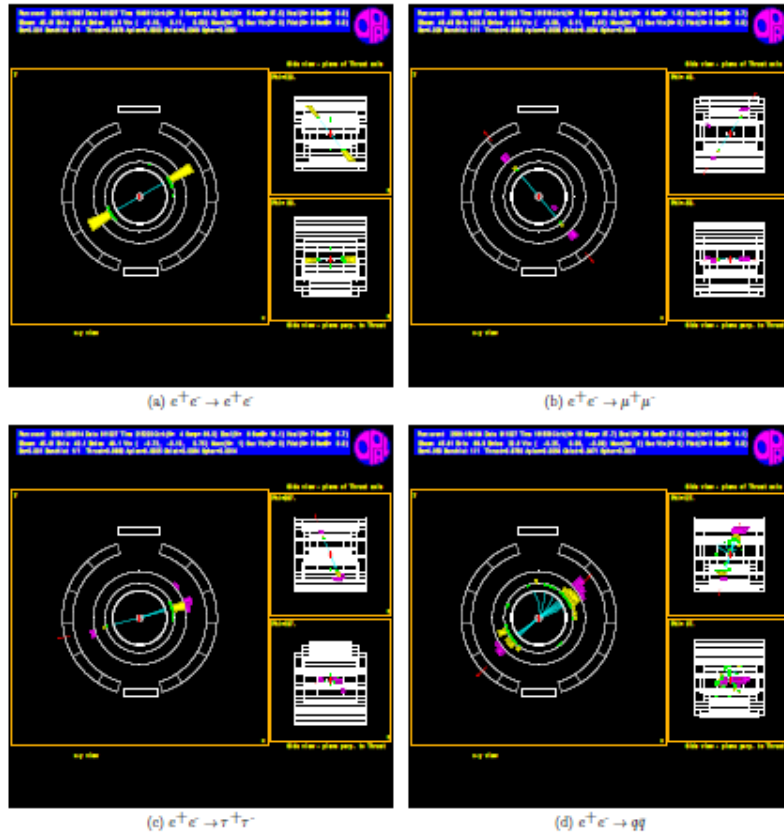
Figure 3.2.: Event displays for different decay modes of e^+e^- [1]

4. Pre-Lab Questions

1. The decay width is given by:

$$\Gamma = \frac{N_c^f \cdot \sqrt{2}}{12\pi} \cdot G_F \cdot M_Z^3 \cdot \left((g_V^f)^2 + (g_A^f)^2\right) \tag{4.1}$$

with

$$g_V^f = I_3^f - 2Q_f \sin^2\theta_W = \text{vector coupling strength}$$
$$g_A^f = I_3^f = \text{axial vector coupling strength} \tag{4.2}$$

where

$$N_c^f = \text{color factor (1 for leptons, 3 for quarks)}$$
$$G_F = \text{Fermi's constant} = 1.16637 \times 10^{-5}\ \text{GeV}^{-2}(\hbar c)^3$$
$$M_Z = 91.182\ \text{GeV}$$
$$I_3^f = \text{third component of weak isospin} \tag{4.3}$$
$$Q_f = \text{electric charge of the fermion}$$
$$\sin^2\theta_W = 0.2312$$

The decay widths for the different processes are given in table 4.1.

Process	N_c^f	I_3^f	Q_f	$\Gamma_f^{calculated}$ /MeV	$\Gamma_f^{literature}$ /MeV
$Z^0 \rightarrow l^+ l^-$ $(l = e, \mu, \tau)$	1	$-\frac{1}{2}$	-1	83.395	83.8
$Z^0 \rightarrow q\bar{q}^-$ (u,c)	3	$+\frac{1}{2}$	$+\frac{2}{3}$	285.358	299
(d,s,b)		$-\frac{1}{2}$	$-\frac{1}{3}$	367.814	378
$Z^0 \rightarrow \nu\bar{\nu}$	1	$+\frac{1}{2}$	0	165.851	167.6

Table 4.1.: Decay width

2. a) The total Z^0 decay width is given by eq. (2.2).

$$\Gamma_{Z^0} = \Gamma_e + \Gamma_\mu + \Gamma_\tau + \Gamma_u + \Gamma_c + \Gamma_d + \Gamma_s + \Gamma_b + \Gamma_{\nu_e} + \Gamma_{\nu_\mu} + \Gamma_{\nu_\tau}$$
$$= 3\Gamma_l + 2\Gamma_{q=u,c} + 3\Gamma_{q=d,s,b} + 3\Gamma_\nu$$
$$= 2.422\ \text{GeV}$$

   b) The hadronic decay width is:

$$\Gamma_{hadron} = \Gamma_u + \Gamma_c + \Gamma_d + \Gamma_s + \Gamma_b$$
$$= 2\Gamma_{q=u,c} + 3\Gamma_{q=d,s,b}$$
$$= 1.67\ \text{GeV}$$

c) The charged decay width is:

$$\Gamma_{lepton} = \Gamma_e + \Gamma_\mu + \Gamma_\tau$$
$$= 3\Gamma_l$$
$$= 0.250 \text{ GeV}$$

d) The neutral decay width is:

$$\Gamma_{neutral} = \Gamma_{\nu_e} + \Gamma_{\nu_\mu} + \Gamma_{\nu_\tau}$$
$$= 3\Gamma_\nu$$
$$= 0.498 \text{ GeV}$$

e) The partial cross-section at the maximum resonance is given by eq. (2.5).

- $\sigma = 2.09$ nb; $f = e, \mu, \tau$
- $\sigma = 7.16$ nb; $f = u, c$
- $\sigma = 9.23$ nb; $f = d, s, b$
- $\sigma = 4.16$ nb; $f = \nu$

3. The broadening in the width can be calculated by adding an extra factor of the particular fermion's partial decay width to eq. (2.2),i.e., $\Gamma_{Z^0}^{new} = \Gamma_{Z^0} + \Gamma_f$. Then the percentage broadening will be $\frac{\Gamma_f}{\Gamma_{Z^0}} \times 100$

- $f = u : \Gamma_{Z^0}^{new} = 2.422 + 0.285 = 2.707$ GeV

  $\implies$ the change in the width of the Z^0 resonance curve would be 11.8%.

- $f = d : \Gamma_{Z^0}^{new} = 2.422 + 0.368 = 2.79$ GeV

  $\implies$ the change in the width of the Z^0 resonance curve would be 15.2%.

- $f = e : \Gamma_{Z^0}^{new} = 2.422 + 0.083 = 2.505$ GeV

  $\implies$ the change in the width of the Z^0 resonance curve would be 3.4%.

- $f = \nu : \Gamma_{Z^0}^{new} = 2.422 + 0.166 = 2.588$ GeV

  $\implies$ the change in the width of the Z^0 resonance curve would be 6.8%.

4. The $e^+e^- \rightarrow e^+e^-$ scattering takes place through both $s-$ and $t-$channels. The s-channel scattering cross-section varies with the scattering angle as $(1 + cos^2\Theta)$ whereas the t-channel varies as $\frac{1}{(1-cos\Theta)^2}$ as shown in fig. 4.1a.
The $e^+e^- \rightarrow \mu^+\mu^-$ decay happens via $s-$channel only as shown in fig. 4.1b.

5. The forward-backward asymmetry is given by eq. (2.6):

$$A_{AB}^f = \frac{3}{4}\frac{F_2}{F_1}$$
$$= \frac{3}{4}\frac{Q_f^2 - 2v_e v_f Q_f Re(\chi) + (v_e^2 + a_e^2)(v_f^2 + a_f^2)|\chi|^2}{-2a_e a_f Q_f Re(\chi) + 4v_e a_e v_f a_f |\chi|^2}$$
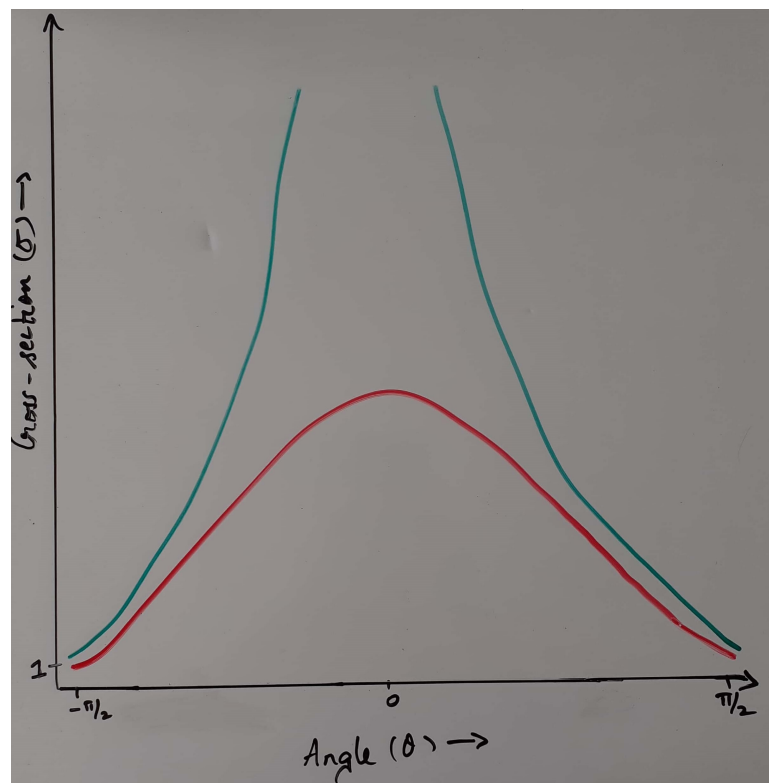
(a) $e^+e^- \rightarrow e^+e^-$

The red line depicts the s-channel scattering and the green line depicts the t-channel scattering
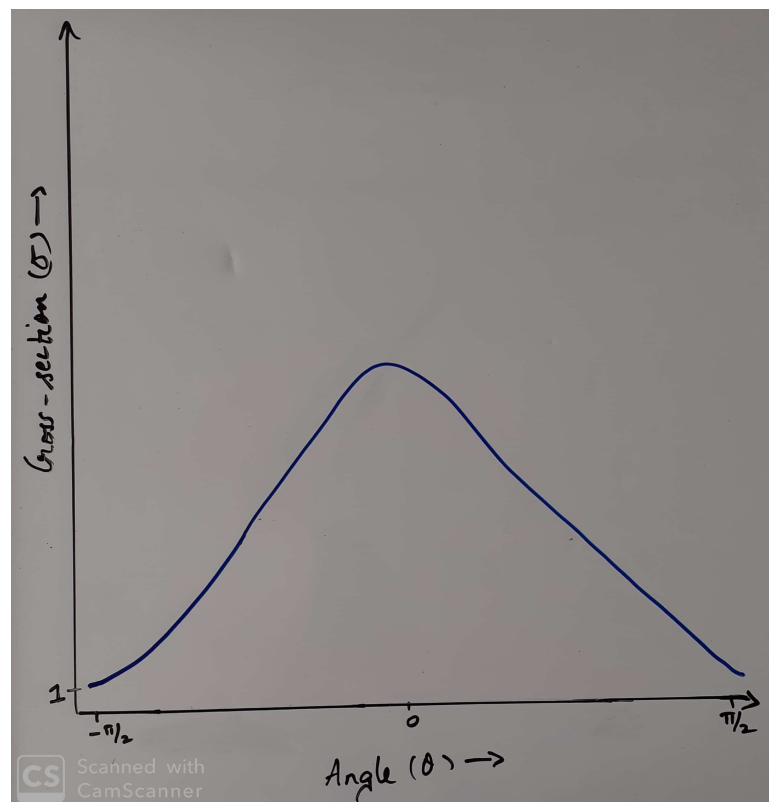
(b) $e^+e^- \rightarrow \mu^+\mu^-$

Figure 4.1.: Expected angular distributions

where $v_f = \dfrac{g_V^f}{2sin\theta_W cos\theta_w} = \dfrac{I_3^f - 2Q_f sin^2\theta_W}{2sin\theta_W cos\theta_W}$

$a_f = \dfrac{g_A^f}{2sin\theta_W cos\theta_W} = \dfrac{I_3^f}{2sin\theta_W cos\theta_W}$

$\chi(s) = \dfrac{s}{(s - M_{Z^0}^2) + is\,\Gamma_{Z^0}/M_{Z^0}}$

$s = E_{CMS}^2$

Here, $f = e = \mu$. The forward-backward asymmetries are given in table 4.2.

E_{CMS} /GeV $\diagdown$ $sin^2\theta_W$	0.21	0.23	0.25
89.225	-0.0937	-0.1639	-0.1949
91.225	0.0762	0.0228	0.0042
93.225	0.2318	0.1965	0.1906

Table 4.2.: Forward-backward asymmetries in the process $e^+e^- \to \mu^+\mu^-$ for the given combinations of center-of-mass energies and Weinberg angles

5. Analysis of Event Displays

The Z^0 was analyzed with the help of the images from GROPE. Pure samples of the e^+e^-, $\mu^+\mu^-$, $\tau^+\tau^-$ and $q\bar{q}$ decay modes with a small number of events were analyzed to obtain their signatures in the detector. This enabled us to obtain approximate cuts to identify the different channels of Z^0 decay. The quantities for which the cuts were determined are:

- `Ctrk(N)` - Number of charged tracks

- `Ctrk(Sump)` - Momentum of all charged tracks

- `Ecal(SumE)` - Total energy in the electromagnetic calorimeter

- `Hcal(SumE)` - Total energy in the hadronic calorimeter

The obtained cuts are shown in table 5.1 and the graphical basis for determining the cuts are shown in fig. 5.1.

Mode of decay	`Ctrk(N)`	`Ctrk(Sump)`	`Ecal(SumE)`	`Hcal(SumE)`
e^+e^-	<5	>30	>80	<2
$\mu^+\mu^-$	<5	>80	<6	<25
$\tau^+\tau^-$	≤5	<80	<60	<25
$q\bar{q}$	>5	>20	>35	>2

Table 5.1.: Approximate cuts determined using the event displays of the pure samples

One mixed sample, 'test2', was analyzed and its events were categorized into different decay modes as shown in table 5.2.
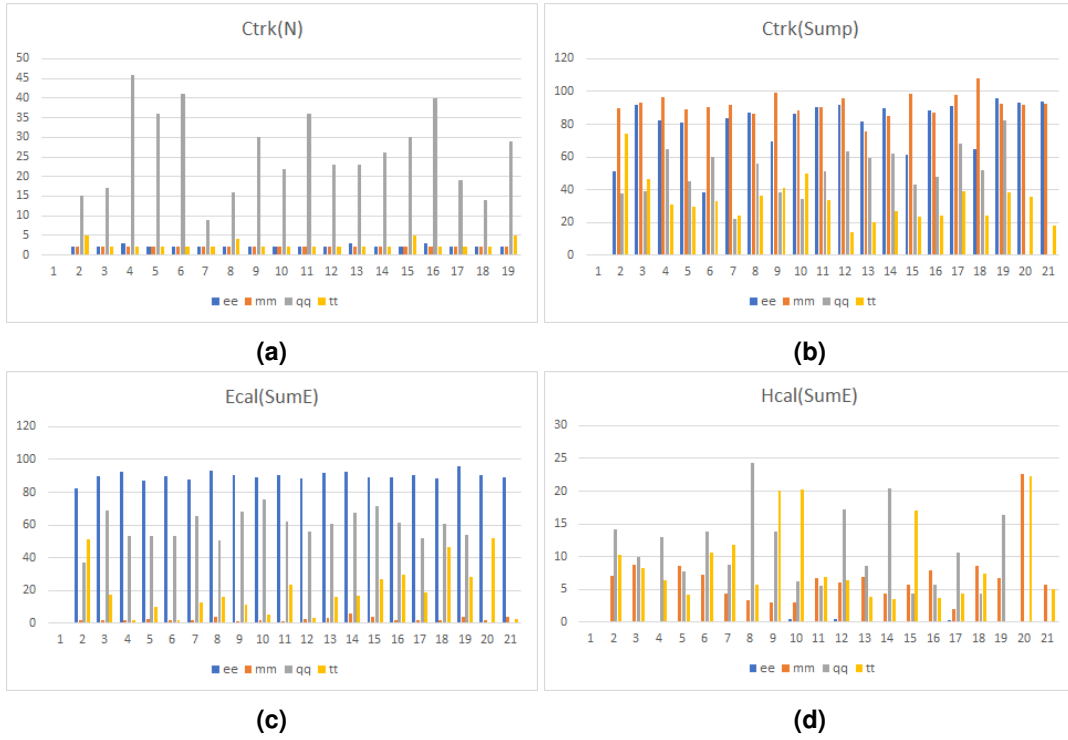
(a)

(b)

(c)

(d)

Figure 5.1.: Bar charts drawn using Excel used to determine cuts

Ctrk(N)	Ctrk(Sump)	Ecal(SumE)	Hcal(SumE)	Decay Mode
45	65.3	51.3	2.4	$q\bar{q}$
44	25.6	47.3	5.2	$q\bar{q}$
2	97	2.2	8.9	$\mu^+\mu^-$
33	24.6	43.4	14.8	$q\bar{q}$
2	95.2	1.3	7.9	$\mu^+\mu^-$
2	22.7	34.4	0	$\tau^+\tau^-$
28	43.8	61.8	12.1	$q\bar{q}$
26	54.7	72.4	1.2	$q\bar{q}$
4	1.6	2.3	0	$\tau^+\tau^-$
2	78.2	90.5	0	e^+e^-
2	106.2	2.6	3.6	$\mu^+\mu^-$
2	90.5	93.2	0	e^+e^-
6	35.4	16	20.1	$\tau^+\tau^-$
2	90.7	92.9	0.6	$\mu^+\mu^-$
2	93.8	1.9	9.4	$\mu^+\mu^-$
2	29.1	21.6	3.8	$\tau^+\tau^-$
4	93.1	92.9	0	e^+e^-
2	97.5	2.5	3.6	$\mu^+\mu^-$
2	3.9	4.2	0	$\tau^+\tau^-$
2	69.4	92.9	0.2	e^+e^-

Table 5.2.: Classification of mixed sample 'test2'

6. Statistical Analysis of Z^0 Decays

The cuts determined from the EventDisplays are not enough to get a precise measurement of real data. To get more accurate cuts, Monte Carlo samples of each of the four decay modes were studied using ROOT. The quantities for which the cuts were determined are:

- Ncharged - Number of charged tracks

- Pcharged - Total scalar sum of track momenta

- E_ecal - Total energy in eletromagnetic calorimeter

- E_hcal - Total energy in hadronic calorimeter

- E_lep - LEP beam energy ($\sqrt{s}/2$)

- cos_thru - cos(polar angle) between beam axis and thrust axis

- cos_thet - cos(polar angle) between incoming positron and outgoing positive particle

6.1. Analysis of Monte Carlo Samples

Four Monte Carlo (MC) samples (pure samples) for the decay of $Z^0 \rightarrow e^+e^-$, $Z^0 \rightarrow \mu^+\mu^-$, $Z^0 \rightarrow \tau^+\tau^-$ and $Z^0 \rightarrow q\bar{q}$ were analyzed. Firstly, the non-physical events were removed by specifying the global cut $[-1 \leq \cos\_thet, \cos\_thru \leq 1]$. The cuts developed previously were then refined for the remaining physical events. We required only s-channel scattering, so the s and t channels were separated with a cut $[-0.5 \leq \cos\_thet \leq 0.4]$ for the e^+e^- decay channel. The optimized cuts are tabulated in table 6.1. The histograms of the MC sample are presented in the appendix.

Decay Channel	Ncharged	Pcharged [GeV]	E_ecal [GeV]	E_hcal [GeV]
e^+e^-	<5	70–100	85–95	<2
$\mu^+\mu^-$	<5	85–100	1–2.5	<9
$\tau^+\tau^-$	<5	10–80	<60	<10
$q\bar{q}$	>5	20–90	35–85	2–40

Table 6.1.: Optimized cuts

The precision of the cuts can be determined with the efficiency matrix. For N_0 events before the cuts and $N_{detected}$ events after the cuts are applied, the efficiency ϵ is defined as:

$$N_{detected} = \epsilon \, N_0 \implies \epsilon = \frac{N_{detected}}{N_0} \tag{6.1}$$

By applying the cuts for one decay channel to all the channels, the efficiency matrix can be determined.

$$\epsilon = \begin{pmatrix} \frac{N_{e-e}}{N_{0,e}} & \frac{N_{m-e}}{N_{0,m}} & \frac{N_{t-e}}{N_{0,t}} & \frac{N_{q-e}}{N_{0,q}} \\ \frac{N_{e-m}}{N_{0,e}} & \frac{N_{m-m}}{N_{0,m}} & \frac{N_{t-m}}{N_{0,t}} & \frac{N_{q-m}}{N_{0,q}} \\ \frac{N_{e-t}}{N_{0,e}} & \frac{N_{m-t}}{N_{0,m}} & \frac{N_{t-t}}{N_{0,t}} & \frac{N_{q-t}}{N_{0,q}} \\ \frac{N_{e-q}}{N_{0,q}} & \frac{N_{m-q}}{N_{0,m}} & \frac{N_{t-q}}{N_{0,t}} & \frac{N_{q-q}}{N_{0,q}} \end{pmatrix}$$

where N_{i-j} means the number of events left in i^{th} channel after cuts of jth channel are applied and $N_{0,i}$ means the number of events in i^{th} channel without any cuts (except the non-physical ones). The error is given by:

$$\Delta\epsilon_i = \sqrt{(1-\epsilon_i)\frac{\epsilon_i}{N_i}}$$

The obtained efficiency matrix is:

$$\epsilon = \begin{pmatrix} 0.956 & 0 & 0.00488 & 0 \\ 0 & 0.859 & 0.00013 & 0 \\ 0.00107 & 0.00049 & 0.912 & 0 \\ 0 & 0 & 0.042 & 0.865 \end{pmatrix} \pm \begin{pmatrix} 0.0014 & 0 & 0.00035 & 0 \\ 0 & 0.0012 & 0.00006 & 0 \\ 0.00021 & 0.00008 & 0.00142 & 0 \\ 0 & 0 & 0.001 & 0.0015 \end{pmatrix}$$

For an unknown data sample, the actual number of physical events $N_{0,data}$ is unknown and only the detected number of events N_{obs} can be found out. To find $N_{0,data}$, the background matrix has to determined. From eq. (6.1),

$$N_0 = \epsilon^{-1} N_{obs}$$

Therefore, the inverse efficiency matrix is required. The error is given by $\Delta\epsilon^{-1} = \epsilon^{-1}\Delta\epsilon\,\epsilon^{-1}$.

$$\epsilon^{-1} = \begin{pmatrix} 1.05 & 0.000003 & -0.0056 & 0 \\ 0.0000002 & 1.164 & -0.00017 & 0 \\ -0.00123 & -0.00062 & 1.096 & 0 \\ 0.000078 & 0.00004 & -0.0696 & 1.5106 \end{pmatrix} \pm \begin{pmatrix} 0.00154 & 0.0000009 & 0.00038 & 0 \\ 0.0000002 & 0.00162 & 0.000076 & 0 \\ 0.00024 & 0.0001 & 0.0017 & 0 \\ 0.000021 & 0.0000072 & 0.0014 & 0.0034 \end{pmatrix}$$

Ideally, the efficiency matrix should be an identity matrix as the cuts of one channel must filter out all the other channels. But practically, this is not the case. This may be because of inaccuracy of the cuts or other statistical and systematic errors.

6.2. Analysis of Data from OPAL

Using the results from the MC samples, we could proceed to analyze real data from OPAL. We analyzed 'data3'. First, the numbers of events in the different decay channels were obtained at different energy intervals. Then, it was corrected using the inverse efficiency matrix. The numbers are given in table 6.2. The error was calculated by Gaussian error propagation, $\Delta N_0 = \sqrt{N_0}$.

Center-of-mass energy ($\sqrt{s}$) [GeV]	e^+e^-	$\mu^+\mu^-$	$\tau^+\tau^-$	$q\bar{q}$
88.47	41	35	37	1728
89.46	173	201	155	7492
90.22	416	675	600	27484
91.22	401	807	606	32717
91.97	54	122	96	5299
92.96	42	74	90	3755
93.71	53	85	75	3709

(a) Number of events observed

Center-of-mass energy ($\sqrt{s}$) [GeV]	e^+e^-	$\mu^+\mu^-$	$\tau^+\tau^-$	$q\bar{q}$
88.47	443 ± 7	41 ± 6	41 ± 6	2610 ± 51
89.46	182 ± 13	234 ± 15	170 ± 13	11317 ± 106
90.22	437 ± 21	786 ± 20	658 ± 26	41517 ± 204
91.22	421 ± 21	939 ± 31	664 ± 26	49422 ± 222
91.97	57 ± 8	142 ± 12	105 ± 10	8005 ± 89
92.96	44 ± 7	86 ± 9	99 ± 10	5672 ± 75
93.71	56 ± 7	99 ± 10	82 ± 9	5603 ± 75

(b) Number of events after correction using efficiency matrix

Table 6.2.: Number of events for different decay modes at different energies

As we can see, the $q\bar{q}$ channel is the most dominant one with more than 90% of the events.

Cross-Section

The reaction cross-section of the final states with *n* events can be calculated using the known reaction cross-section of another event by means of the luminosity (*L*). In the LEP, high center-of-mass energies are used and the higher order Feynman diagrams also contribute significantly to the cross-section. So, the radiative corrections have to be taken into account. Therefor the cross-section is given by:

$$\sigma = \frac{N}{\int L dt} + \text{Radiative correction}$$

(6.2)

The error was calculated by Gaussian error propagation. The radiative corrections and integrated luminosities ($\int L dt$) were taken from [1]. The cross-sections are given in table 6.3. The highest cross-section for all channels is between 90.22 and 91.22 GeV which is close to the Z^0 mass. The disparency may be due to mistakes made in determining the cuts leading to incomplete filtering of different channels.

Forward-Backward Asymmetry

The forward-backward asymmetry of the muon final states was calculated by measuring the number of events in the forward ($\cos\theta > 0$) and backward ($\cos\theta < 0$) directions. Using eq. (2.6):

$$A_{FB}^f = \frac{N_F - N_B}{N_F + N_B} + A_{FB} \text{ correction}$$

$\sqrt{s}$ [GeV]	σ [nb]			
	e^+e^-	$\mu^+\mu^-$	$\tau^+\tau^-$	$q\bar{q}$
88.47	0.20 ± 0.03	0.19 ± 0.03	0.19 ± 0.03	8.48 ± 0.18
89.46	0.53 ± 0.04	0.63 ± 0.04	0.51 ± 0.04	25.07 ± 0.32
90.22	1.16 ± 0.06	1.81 ± 0.05	1.57 ± 0.06	84.20 ± 0.85
91.22	0.72 ± 0.04	0.97 ± 0.03	0.84 ± 0.03	34.56 ± 0.30
91.97	0.33 ± 0.05	0.51 ± 0.04	0.43 ± 0.04	20.92 ± 0.30
92.96	0.12 ± 0.02	0.24 ± 0.03	0.28 ± 0.03	16.44 ± 0.28
93.71	0.01 ± 0.00	0.08 ± 0.01	0.05 ± 0.01	7.40 ± 0.12

Table 6.3.: Cross-section at different center-of-mass energies

The corrections were taken from [1]. At the Z^0 resonance, the asymmetry can be approximated as:

$$A_{FB} = 3(1 - 4\sin^2\theta_W)$$

following eq. (2.7). The forward-backward asymmetry for the corresponding energies and the Weinberg angle is given in table 6.4.

$\sqrt{s}$ [GeV]	N_F	N_B	A_{FB}	$sin^2\theta_W$
88.47	13 ± 22	3.61 ± 4.69	-0.236 ± -0.224	
89.46	79 ± 87	8.89 ± 9.33	0.061 ± 0.139	
90.22	319 ± 356	17.86 ± 18.87	-0.038 ± -0.038	0.222 ± 0.014
91.22	406 ± 399	20.15 ± 19.97	0.027 ± 0.155	
91.97	65 ± 57	8.06 ± 7.55	0.096 ± 0.187	
92.96	46 ± 28	6.78 ± 5.29	0.305 ± 0.211	
93.71	47 ± 38	6.86 ± 6.16	0.200 ± 0.291	
MC Sample (91.22)	23501 ± 23174	153.30 ± 152.23	0.025 ± 0.024	0.227 ± 0.011

Table 6.4.: Forward-backward asymmetry and Weinberg angle

The calculated Weinberg angle agrees with the theoretical value 0.2312 by 1-sigma deviation.

Lepton Universality

Lepton universality predicts that the cross-sections of all leptons must be equal at the Z^0 resonance. The calculated cross-sections of leptons at the peak energy are:

$$\sigma_e = 1.16 ± 0.06$$

$$\sigma_\mu = 1.81 ± 0.05$$

$$\sigma_\tau = 1.57 ± 0.06$$

The differences may be because of the inaccuracy of the cuts and other systematic uncertainties.
The ratio between the cross-section of hadron to lepton gives a clearer picture about lepton universality. The ratios are:

$$R_e = 72.59 ± 3.83$$

$$R_\mu = 46.52 ± 1.37$$

$$R_\tau = 53.63 \pm 2.12$$

The values are significantly different from each other and also compared to the theoretical values calculated in the pre-lab questions meaning our cuts were probably not optimized correctly.

6.3. Breit-Wigner Fit of Cross Section

The cross-sections can be described by a Breit-Wigner distribution of the form eq. (2.4). The cross-section of the different decay modes were plotted against the center-of-mass energy and fitted with a Breit-Wigner distribution as shown in fig. 6.1. We used the best-fit results. The parameters of the fit

(a) $Z^0 \to e^+e^-$

(b) $Z^0 \to \mu^+\mu^-$

(c) $Z^0 \to \tau^+\tau^-$

(d) $Z^0 \to q\bar{q}$
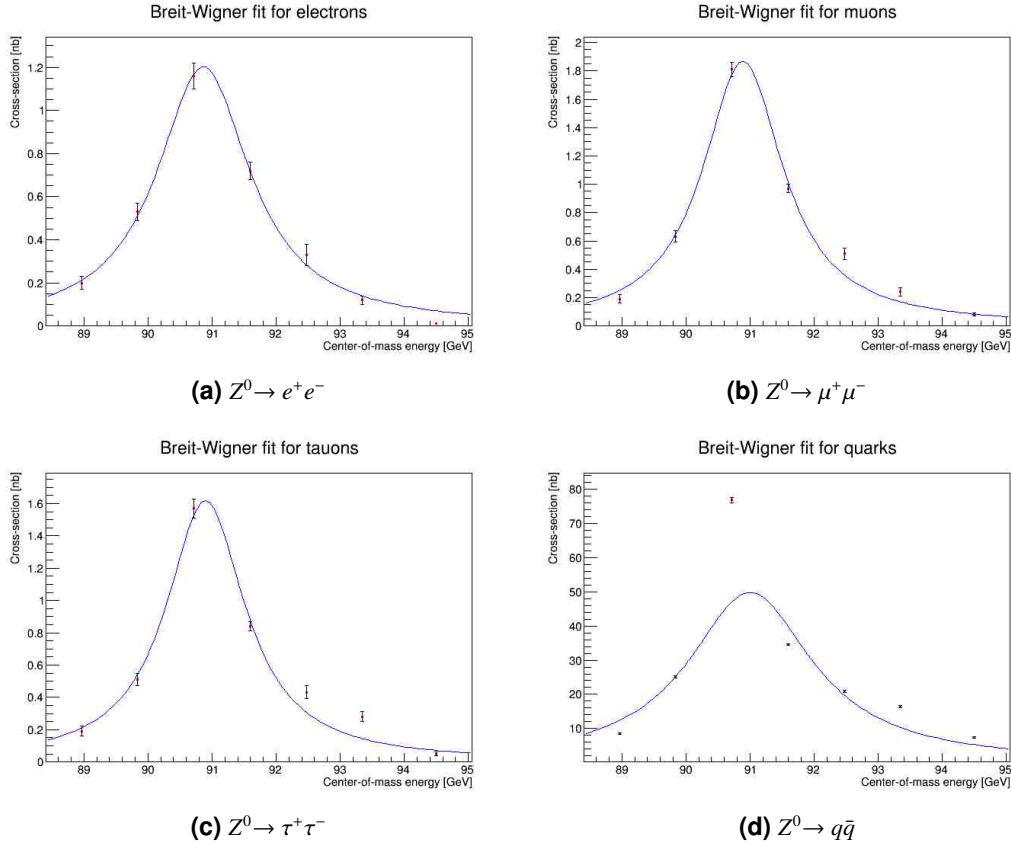
Figure 6.1.: Breit-Wigner fit to the cross-section

are given in table 6.5.

Reduced chi-squared test was done to measure the goodness of the fit. It is the chi-square (weighted sum of squared deviations) per degree of freedom. The number of degrees of freedom is the number of data points minus the number of parameters which is 3 for e^+e^- and 4 for the other channels.

A good fit is one with $\frac{\chi^2}{N_{dof}} = 1$. But this is seldom the case. $\frac{\chi^2}{N_{dof}} > 1$ means the fit has not fully captured the data and that the error has been underestimated. On the other hand, $\frac{\chi^2}{N_{dof}} < 1$ means that the fit is over-fitting the data by fitting noise and the error has been overestimated [2]. The peak cross-section obtained from the fit is comparable with the results obtained previously in table 6.3 within two standard deviations.

Decay mode	σ^{peak} [nb]	Γ_Z [GeV]	M_Z [GeV]	χ^2/N_{dof}
e^+e^-	1.204 ± 0.059	1.771 ± 0.056	90.873 ± 0.038	0.742
$\mu^+\mu^-$	1.869 ± 0.056	1.531 ± 0.056	90.896 ± 0.020	0.642
$\tau^+\tau^-$	1.618 ± 0.066	1.511 ± 0.070	90.905 ± 0.023	0.914
$q\bar{q}$	49.809 ± 0.848	2.366 ± 0.043	91.016 ± 0.012	6.948

Table 6.5.: Fit parameters

The partial width and mass of Z^0 was then found by taking the mean:

$$\Gamma_Z = (1.795 \pm 0.067) \text{ GeV}$$

$$M_Z = (90.922 \pm 0.023) \text{ GeV}$$

The partial widths of different channels calculated using eq. (2.5) are:

$$\Gamma_e = (43.129 \pm 0.146) \text{ MeV}$$

$$\Gamma_\mu = (78.719 \pm 3.152) \text{ MeV}$$

$$\Gamma_\tau = (68.147 \pm 3.318) \text{ MeV}$$

$$\Gamma_q = (1049.148 \pm 33.102) \text{ MeV}$$

The partial widths are significantly smaller than the ones calculated in the pre-lab questions (question 2). The mistakes made in determining the cuts are reflected here.

Number of generations of Light Neutrinos

Using eq. (2.2), the number of generations of light neutrinos, n can be determined. Assuming that the decay width of quarks is the average of all the 5 types of quarks, the decay width of Z^0 is:

$$n\Gamma_\nu = \Gamma_{Z^0} - \Gamma_e - \Gamma_\mu - \Gamma_\tau - \Gamma_q$$
$$= 555.857 \pm 40.785$$

The partial decay width of neutrinos is given as 167.6 MeV in [1]. Then,

$$n = \frac{555.857 \pm 40.785}{167.6} = (3.317 \pm 0.243)$$

This is in agreement with the theoretical value within 2-sigma error.

Systematic Uncertainties

The difference between the theoretical, calculated and experimental values are caused by several known and unknown systematic errors. Error in analysis and calculations are known errors which can be further corrected. Error in calibration of the detector, detector and MC efficiency, and other external parameters is unknown to us.

7. Conclusion

We analyzed the data from OPAL and determined the cross-sections, decay width, forward-backward asymmetries and the number of generations of light neutrinos. This was done in three main steps. First, we determined approximate cuts using the images from GRope. Then we used Monte Carlo sample of pure events and determined precise cuts for each of the four decay channels. Finally, real data from OPAL was analyzed and the necessary quantities were measured both by calculations and Breit-Wigner test. There were some significant differences between the theoretical, calculated and graphical methods. This is due to the systematic errors arising because of improper optimization of cuts and other unknowns.

A. Histograms
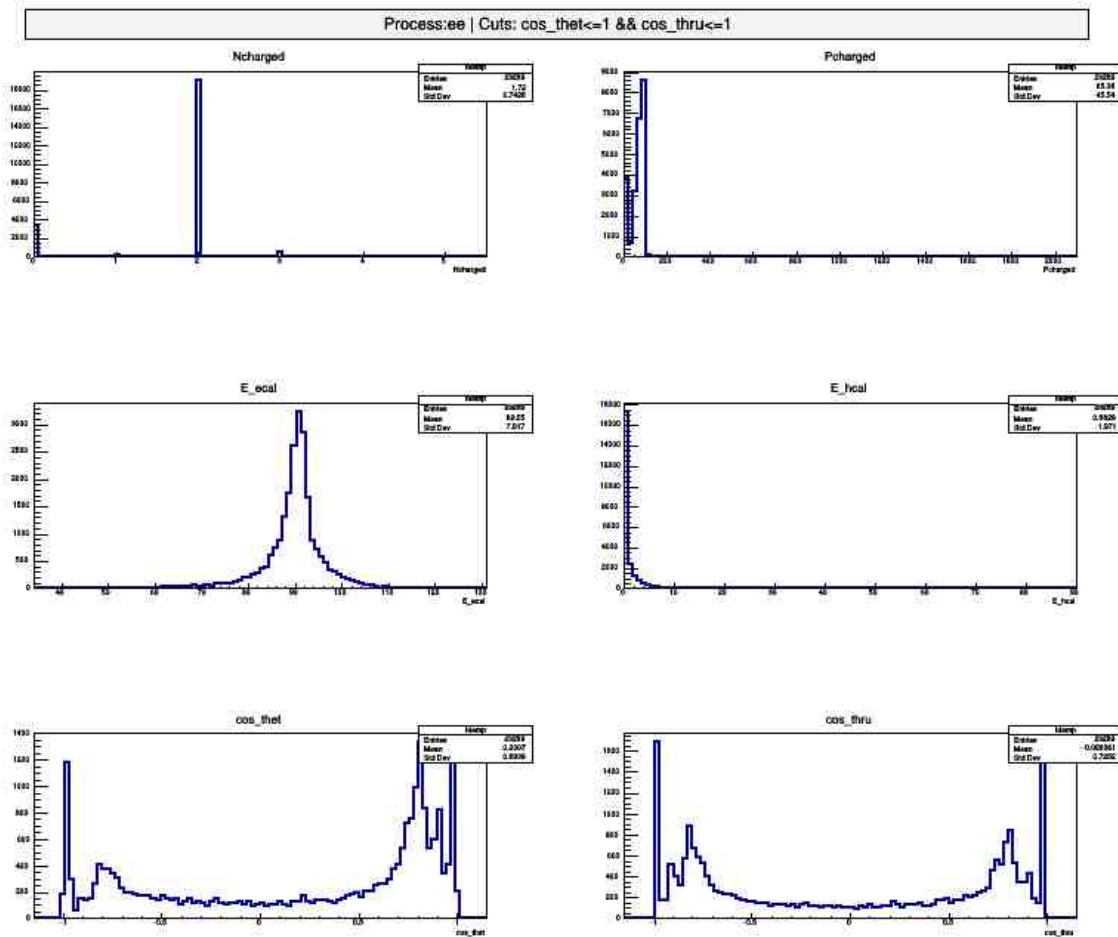
Figure A.1.: $Z^0 \rightarrow e^+ e^-$ without cuts
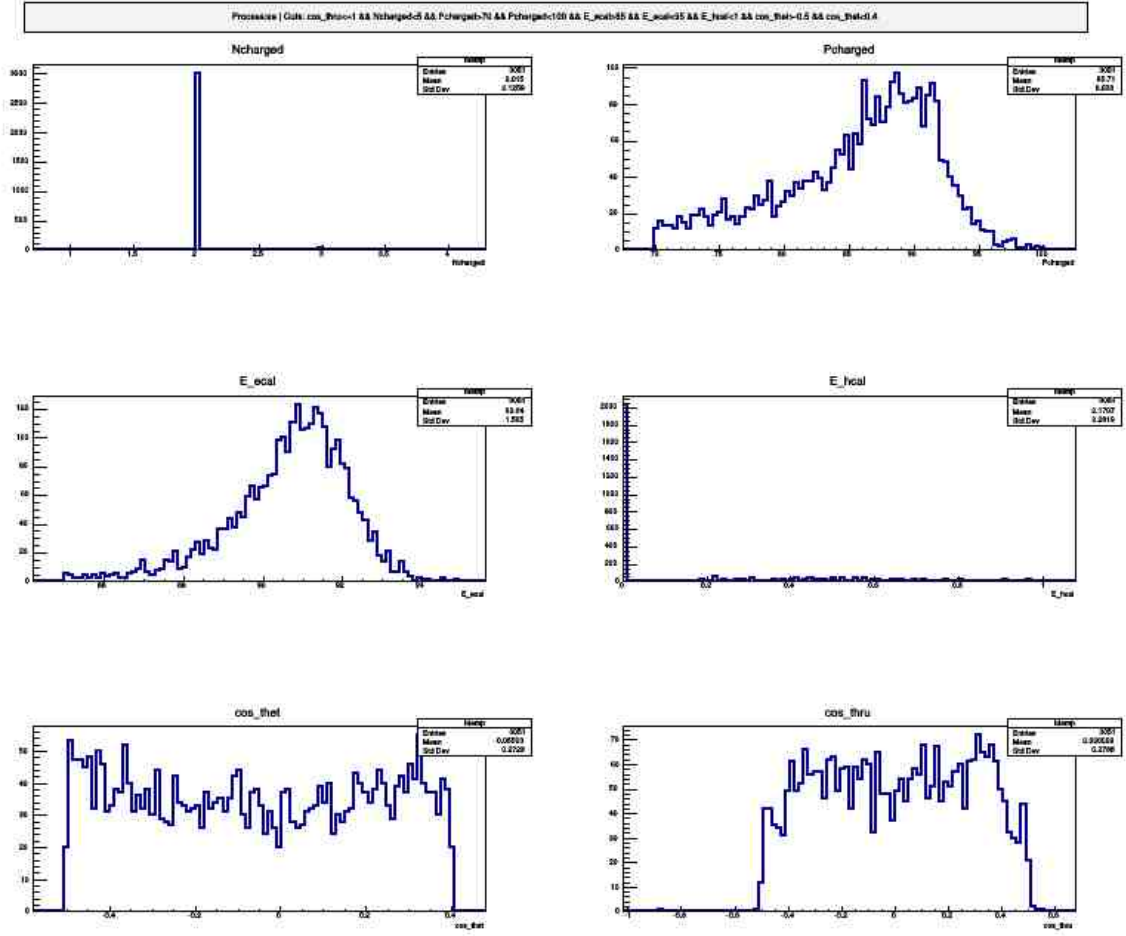
Figure A.2.: $Z^0 \rightarrow e^+ e^-$ with cuts applied
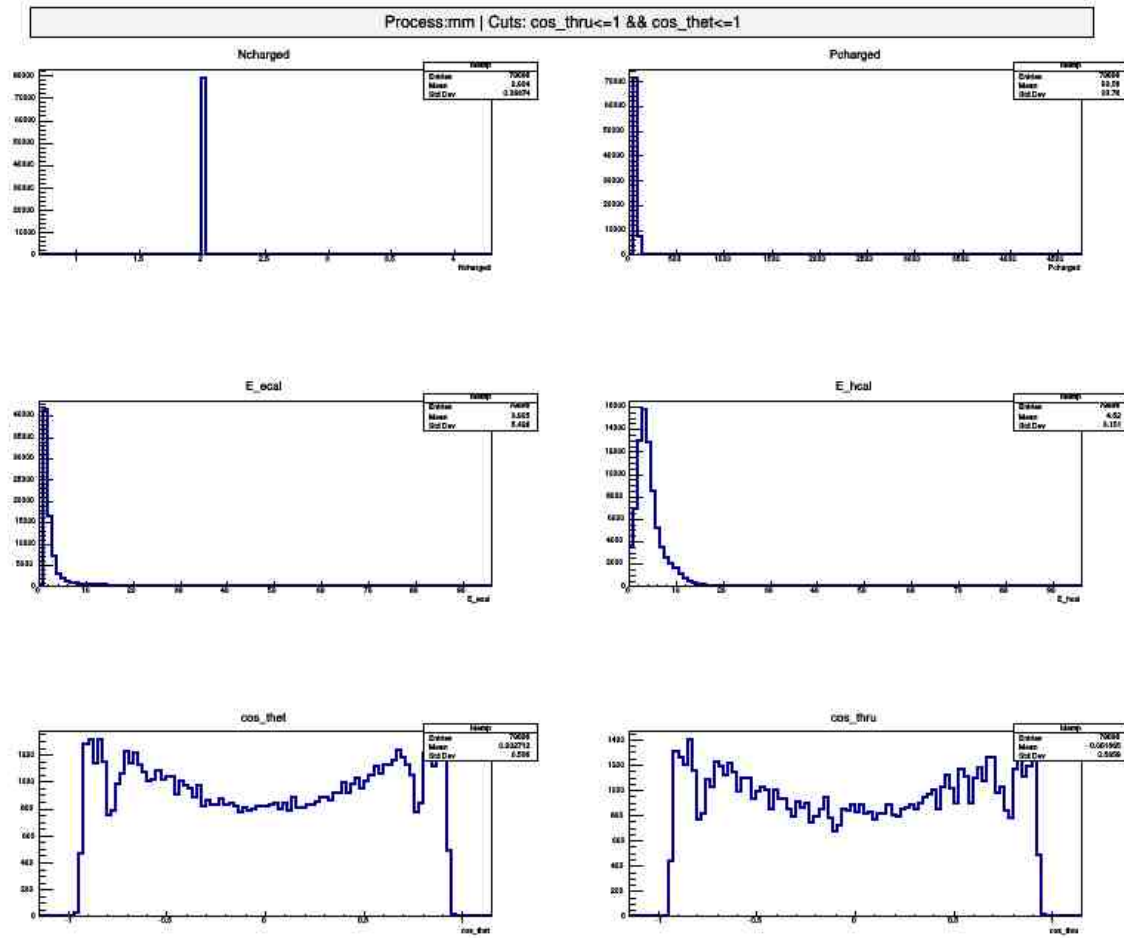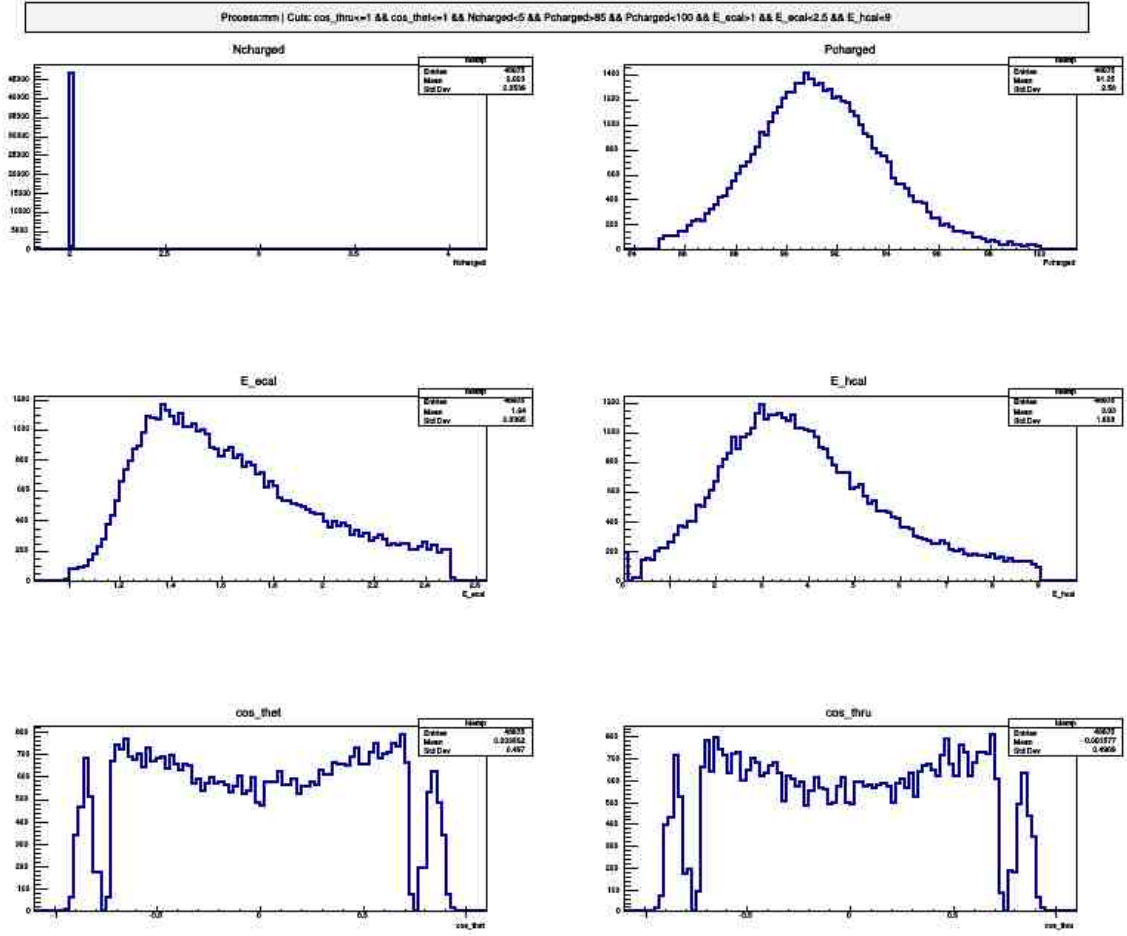
Figure A.3.: $Z^0 \rightarrow \mu^+\mu^-$ without cuts
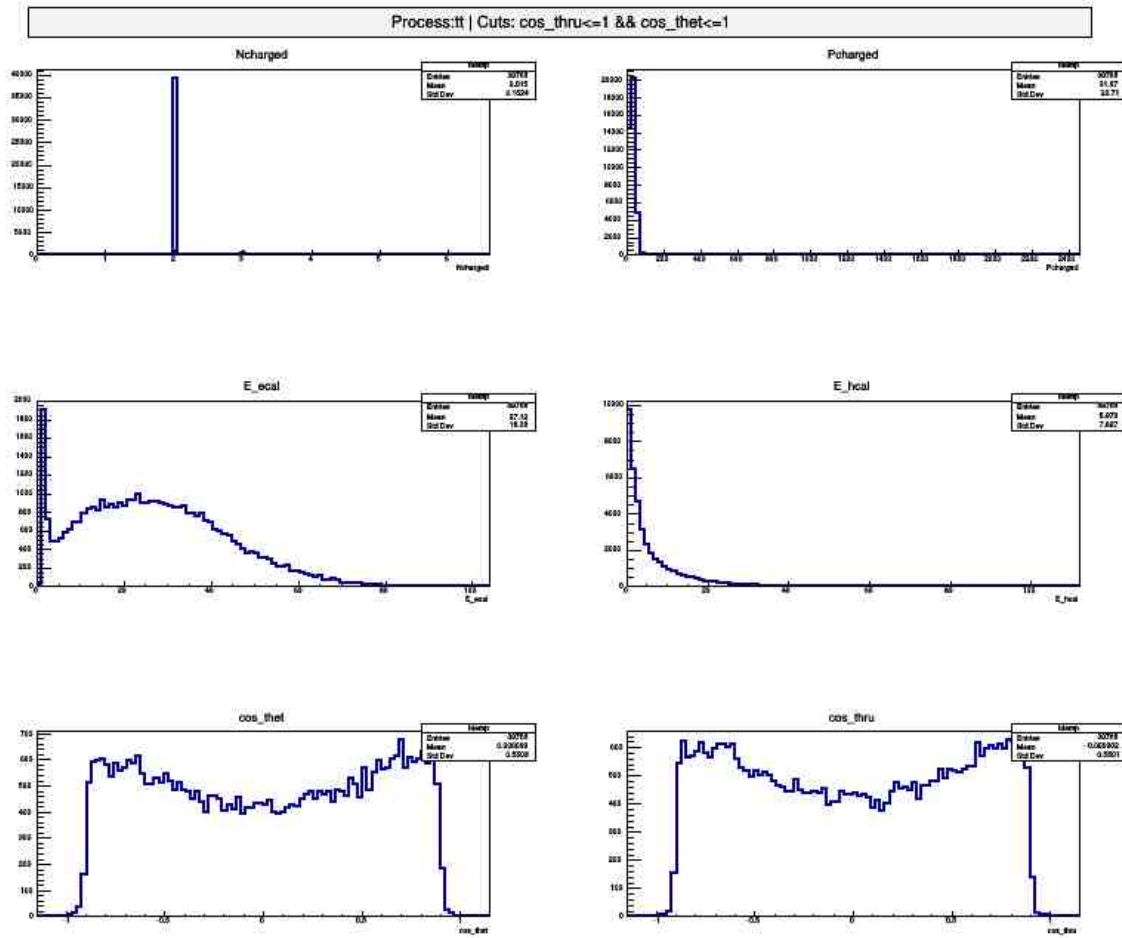
Figure A.4.: $Z^0 \rightarrow \mu^+ \mu^-$ with cuts applied

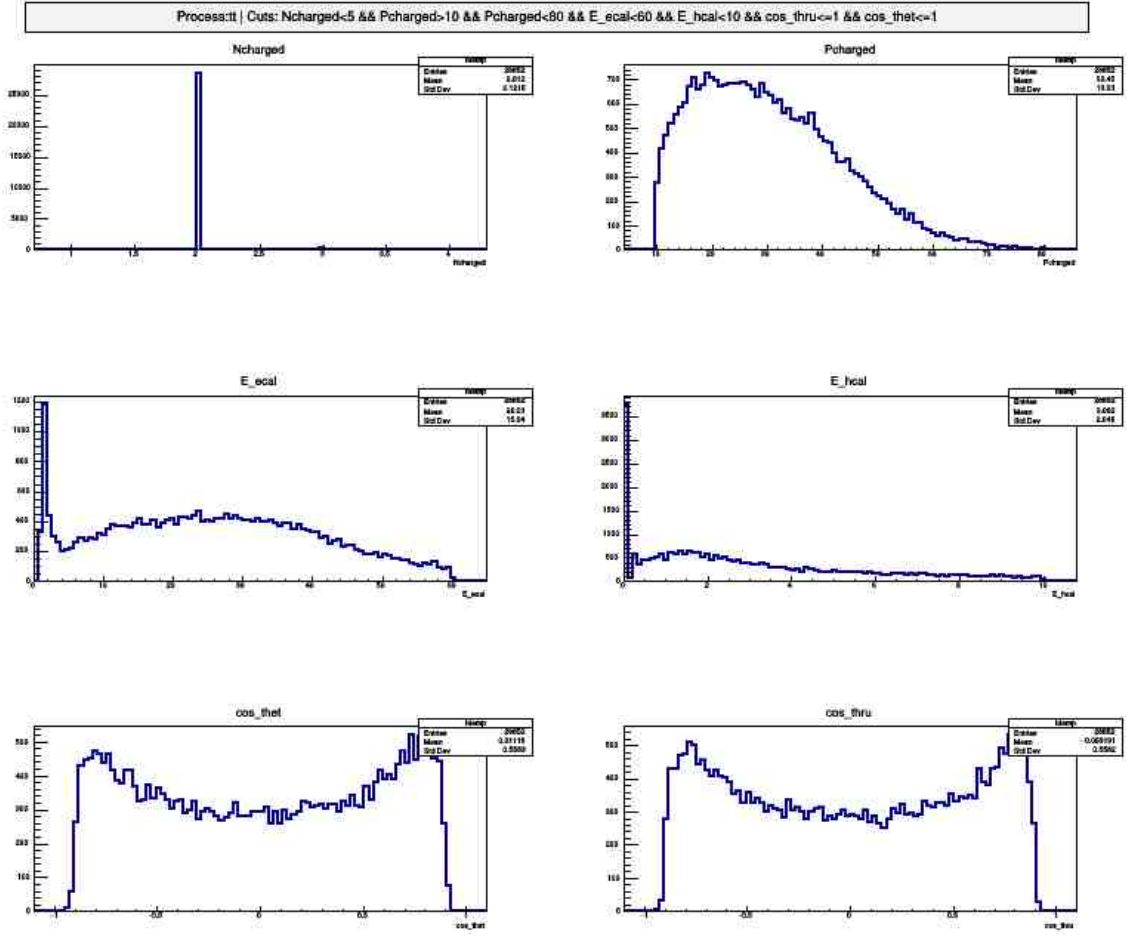**Figure A.5.:** $Z^0 \rightarrow \tau^+\tau^-$ without cuts

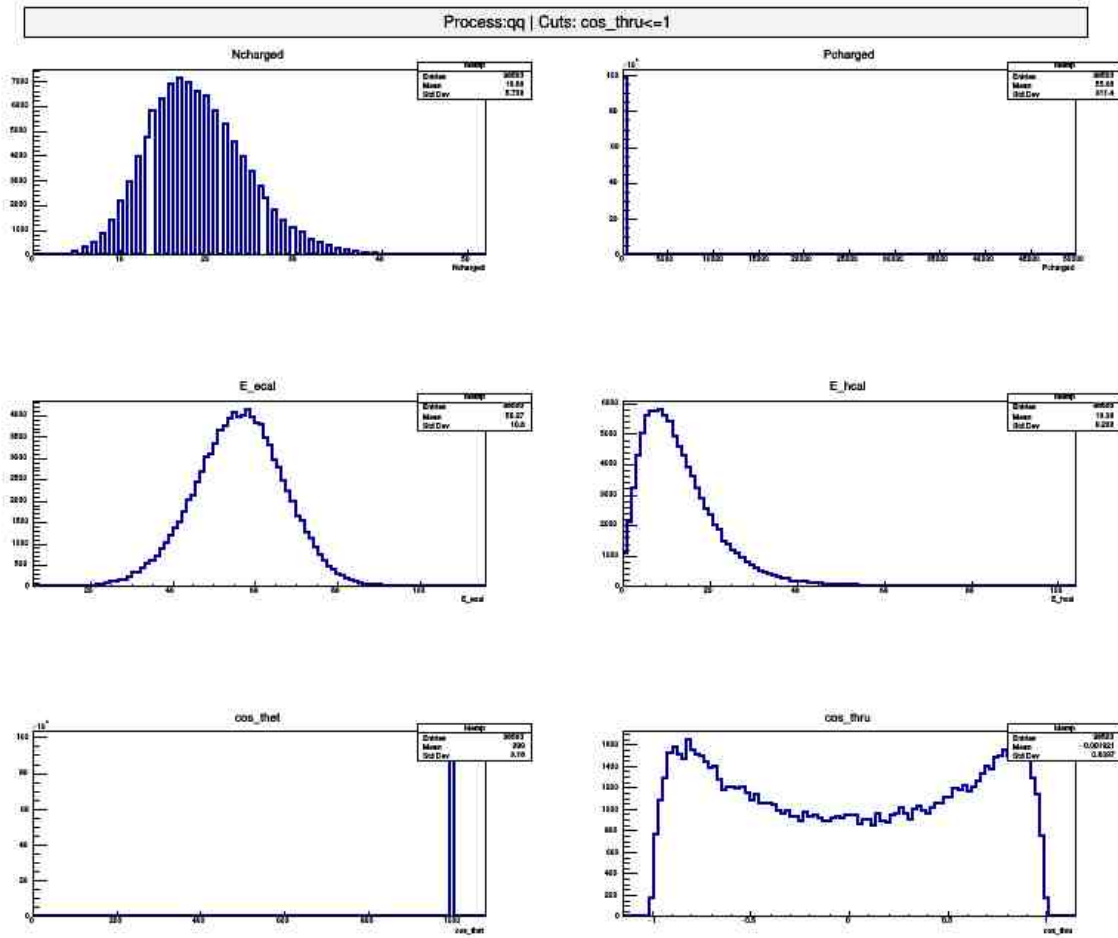**Figure A.6.:** $Z^0 \rightarrow \tau^+ \tau^-$ with cuts applied

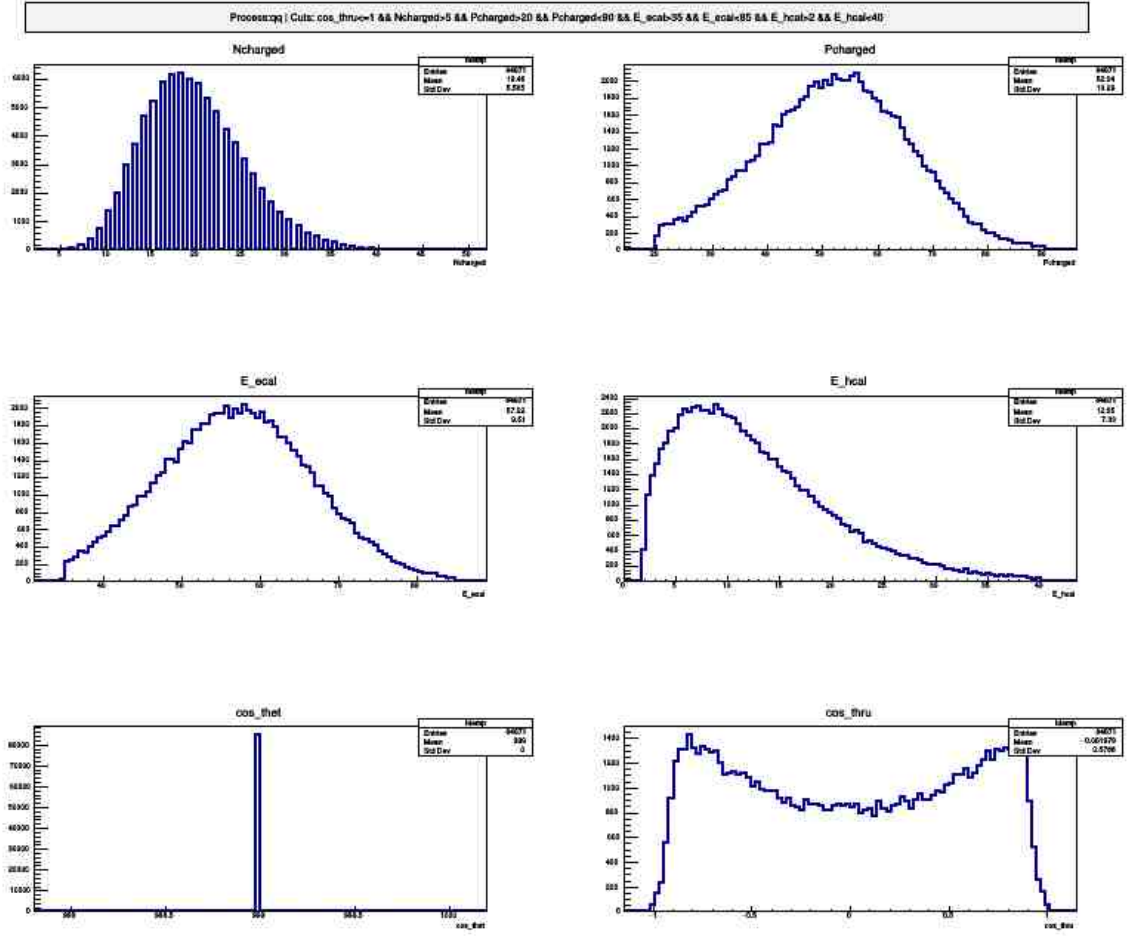**Figure A.7.:** $Z^0 \rightarrow q\bar{q}$ without cuts

Figure A.8.: $Z^0 \rightarrow q\bar{q}$ with cuts applied

Bibliography

[1] *E213 - Analysis of Z^0 Decay*: Script, 2019

[2] *https://en.wikipedia.org/wiki/Reduced_chi-squared_statistic*